ELSEVIER

Journal of Fluids and Structures 24 (2008) 680–699

JOURNAL OF FLUIDS AND STRUCTURES

www.elsevier.com/locate/jfs

Numerical investigation on flow around circular cylinders in tandem arrangement at a subcritical Reynolds number

T. Kitagawa[a,*], H. Ohta[b]

[a]*EcoTopia Science Institute, Nagoya University, Furo-cho, Chikusa-ku, Nagoya 464-8603, Japan*
[b]*Toyota Boshoku Corporation, 1-1 Toyota-cho, Kariya, Aichi 448-8651, Japan*

Received 11 September 2006; accepted 28 October 2007
Available online 4 March 2008

Abstract

Three-dimensional fluid computations have been performed to investigate the flows around two circular cylinders in tandem arrangements at a subcritical Reynolds number, $Re = 2.2 \times 10^4$. The center-to-center space between the cylinders was varied from twice the cylinder diameter to five times that, and the flows and fluid-dynamic forces obtained from the simulations are compared with the experimental results reported in the literature. Special attention is paid to the characteristics of the vortices shed from the upstream cylinder such as the convection, the impingement onto the downstream cylinder and the interaction with the vortices from the downstream cylinder. The effects of the vortices from the upstream cylinder on the fluid-dynamic forces acting on the downstream cylinder are discussed.

Keywords: Circular cylinders in tandem arrangement; Computational fluid dynamics; Vortex shedding

1. Introduction

Numerous studies have been carried out to investigate the flows around circular cylinders in various arrangements and the fluid-dynamic forces acting on them. This is important in many engineering applications because of the need to prevent accidents and disasters. In particular, considerable attention has been paid to the flow around a pair of circular cylinders. This is not only because understanding the flow around two circular cylinders is fundamental to understanding the flow around multiple cylinders in complex arrangements, but also because the flow interference between the two circular cylinders causes a wake-induced vibration [see e.g., Bokaian and Geoola, 1984]. Comprehensive reviews on the flows around two circular cylinders and the wake-induced vibrations were presented by Zdravkovich (1985, 1987, 2003). Extensive investigations on the flow around two circular cylinders and their fluid-dynamic forces have been performed mainly through experimental approaches: e.g., Bearman and Wadcock (1973), King and Johns (1976), Kiya et al. (1980), Igarashi (1981, 1984), Williamson (1985), Sun et al. (1992), Zhang and Melbourne (1992), Gu and Sun (1999) and Sumner et al. (2000, 2005). Sumner et al. (2005) showed that the flow around two circular cylinders can broadly be classified into fourteen distinct patterns with respect to the angle of incidence and the spacing between the cylinders.

*Corresponding author. Tel.: +81 52 789 5918; fax: +81 52 789 3734.
E-mail address: kitagawa@civil.nagoya-u.ac.jp (T. Kitagawa).

0889-9746/$ - see front matter © 2007 Elsevier Ltd. All rights reserved.
doi:10.1016/j.jfluidstructs.2007.10.010

Numerical investigations on the flows around a pair of circular cylinders have also been reported. A limited number of these studies can be found in the literature, and some of them are mentioned in the following discussion. For the flow around two stationary circular cylinders, using the finite-element method (FEM), Mittal et al. (1997) performed 2-D numerical simulations at Reynolds numbers of 10^2 and 10^3. In the case of the tandem arrangement with the center-to-center length ratio (center-to-center length to cylinder diameter, L/D) = 2.5, vortices were not formed from the upstream cylinders at $\mathrm{Re} = 10^2$, but were observed at $\mathrm{Re} = 10^3$. It has been shown experimentally that no distinct vortex is shed from the upstream cylinder if L/D is less than 3–4, i.e., the flow pattern simulated at $\mathrm{Re} = 10^3$ was not consistent with the experimental results. They mentioned that this critical spacing could be sensitive to the value of Re. Meneghini et al. (2001) investigated the flow around two circular cylinders in tandem and side-by-side arrangements at $\mathrm{Re} = 10^2$ and 2×10^2 using a 2-D FEM. The simulated flows were similar to those of experiments around the same Re. In the cases of side-by-side arrangements with cylinder-gaps smaller than $2D$, the 'flopping phenomenon' (Williamson, 1985) was successfully simulated: the drag forces of the cylinders increased and a repulsive force between the cylinders occurred as the wake was deflected to one of the cylinders. Jester and Kallinderis (2003) simulated the flows around two circular cylinders in various arrangements at $\mathrm{Re} = 80$ and 10^3 with a 2-D FEM. An important issue in their results is the characteristic of the fluid forces acting on the cylinders in the cases of tandem arrangements at $\mathrm{Re} = 10^3$. The hysteretic effects of the fluid forces were observed in the range of $2 < L/D < 2.5$: the drag coefficients of the upstream and downstream cylinders took different values, depending on whether L/D slowly increased from 1.9 or decreased from 2.5. However, the upper L/D of the hysteresis range differed from the experimentally obtained values of 3–3.8. Akbari and Price (2005) numerically studied the flow patterns around staggered cylinder pairs at $\mathrm{Re} = 8 \times 10^2$, mainly comparing with the results of flow visualizations. The flow fields were simulated using a 2-D vortex method, and the simulated flows almost agreed with the results of the dye-injection flow visualization experiments by Sumner et al. (2000). On the other hand, for elastically supported circular cylinders, Mittal and Kumar (2001) carried out FEM simulations on the flow around two circular cylinders of $L/D = 5.5$, in which the flow at $\mathrm{Re} = 100$ and the cylinder response motions excited by the fluid forces were computed interactively. The response trajectories of the cylinders under the wake-induced vibrations were obtained. It was observed that the trajectories of the downstream cylinder in the case of the tandem arrangement resembled a figure-of-eight, but in the case of a staggered arrangement where the downstream cylinder positioned by $0.7D$ in the transverse direction, the trajectory of the downstream cylinder had an oval shape.

As described above, numerical investigations on flows around two circular cylinders have been performed recently. Most of these numerical studies, however, employed a 2-D analysis and investigated the flow characteristics at low Re (less than 10^3). On the contrary, many experimental studies have been undertaken at Re higher than those at which the numerical studies have been tried. In practice Re of flows around many structures are much higher, in which case the effects of 3-D turbulence are predominant in the flows and have a significant consequence upon the fluid-dynamic forces. It is well known that, even for a single cylinder, at high Re, the fluid-dynamic characteristics obtained from 2-D flow computations deviate from those of experimental results; in the case of multiple cylinders, the 3-D flow computations are required in a practical sense. In this study, focusing on the flows around two stationary circular cylinders in tandem arrangements in the range of $2 \leqslant L/D \leqslant 5$ at a subcritical Reynolds number, 3-D fluid-dynamic computations are carried out. The Reynolds number is set to 2.2×10^4, equal to that at which Igarashi (1981) measured the Strouhal number of the flow around circular cylinders in tandem arrangements. Comparing with results of previous experimental studies, the characteristics of the flows and the fluid-dynamic forces obtained from the computations are discussed. In particular, the behavior of the vortices shed from the upstream cylinder and the effects of those vortices on the fluid-dynamic forces of the downstream cylinder are investigated.

2. Computational method

2.1. Algorithm

The large eddy simulation (LES) with the Smagorinsky subgrid-scale model was employed. The incompressible Navier–Stokes equation and the equation of continuity in nondimensional form are

$$\frac{\partial u_i}{\partial t} + u_j \frac{\partial u_i}{\partial x_j} = -\frac{\partial P}{\partial x_i} + 2\frac{\partial}{\partial x_i}\left(\frac{1}{\mathrm{Re}} + \frac{1}{\mathrm{Re}_t}\right) S_{ij}, \tag{1}$$

$$\frac{\partial u_i}{\partial x_i} = 0, \tag{2}$$

where u_i is the velocity component of grid scale, and P is the sum of the grid-scale pressure and the residual stress, $S_{i,j}$ is the strain-rate tensor on the grid-scale velocity components,

$$S_{ij} = \frac{1}{2}\left(\frac{\partial u_i}{\partial x_j} + \frac{\partial u_j}{\partial x_i}\right). \tag{3}$$

The subgrid-scale eddy-viscosity, $1/\mathrm{Re}_t$, in Eq. (1) is expressed as

$$\frac{1}{\mathrm{Re}_t} = (C_s \Delta)^2 \sqrt{2 S_{ij} S_{ij}}. \tag{4}$$

In Eq. (4), Δ is the filter width and was given as the cube-root of grid volume, and the Smagorinsky constant, C_s, was set to 0.1 in this study. Additionally, near the cylinder surface, the van Driest function,

$$f_s = 1 - \exp\frac{-y^+}{A^+} \tag{5}$$

was used in Eq. (4). In Eq. (5), $y^+ = y u_\tau / v$ and $A^+ = 25$.

Eqs. (1) and (2) were transformed into a computational coordinate system of ξ^k ($k = 1, 2, 3$), and the contravariant component of the velocity

$$U^k = \frac{\partial \xi^k}{\partial x_i} u_i \tag{6}$$

was applied to the advection term in Eqs. (1) and (2). These substitutions yield

$$\frac{\partial u_i}{\partial t} + \frac{1}{J}(JU^k)\frac{\partial u_i}{\partial \xi^k} = -\frac{\partial \xi^k}{\partial x_i}\frac{\partial P}{\partial \xi^k} + \frac{1}{J}\left(\frac{1}{\mathrm{Re}} + \frac{1}{\mathrm{Re}_t}\right)\frac{\partial}{\partial \xi^k}\left(\gamma^{kl}\frac{\partial u_i}{\partial \xi^l}\right), \tag{7}$$

$$\frac{1}{J}\frac{\partial (JU^k)}{\partial \xi^k} = 0, \tag{8}$$

where J is the Jacobian and

$$\gamma^{kl} = J\frac{\partial \xi^k}{\partial x_m}\frac{\partial \xi^l}{\partial x_m}. \tag{9}$$

Eqs. (7) and (8) were discretized with the finite-difference method (FDM) in the collocated grid system (Rhie and Chow, 1983; Kajishima et al., 1998), and were solved by the simplified marker and cell (SMAC) method (Amsden and Harlow, 1970). The following expressions are used for FDM discretization hereafter:

$$\delta_i f = -f_{i-\frac{1}{2},j,k} + f_{i+\frac{1}{2},j,k}, \quad \delta'_i f = \frac{-f_{i-1,j,k} + f_{i+1,j,k}}{2}, \tag{10,11}$$

$$\overline{f}^i = \frac{f_{i-\frac{1}{2},j,k} + f_{i+\frac{1}{2},j,k}}{2}. \tag{12}$$

The second-order Adams–Bashforth method and the Crank–Nicolson method were applied to the advection term and the diffusion term of the incompressible Navier–Stokes equation, respectively. The predicted velocity in the SMAC method, u_i^P, is obtained by solving

$$u_i^P - \frac{\Delta t}{2J}\left(\frac{1}{\mathrm{Re}} + v_{sgs}\right)\delta_k\left(\overline{\gamma^{kl}}^{kl}\delta_l \overline{u_i^P}^{kl}\right) = u_i^n + \frac{\Delta t}{2J}\left(\frac{1}{\mathrm{Re}} + \frac{1}{\mathrm{Re}_t}\right)\delta_k\left(\overline{\gamma^{kl}}^{k}\delta_l \overline{u_i^n}^{kl}\right) - \Delta t \frac{\partial \xi^k}{\partial x_i}\overline{\delta_k P^n}^{k} + \Delta t \frac{3A_i^n - A_i^{n-1}}{2}, \tag{13}$$

where Δt is the nondimensional time step and was set to 0.002, and A_i denotes the advection term and a third-order upstream scheme was employed:

$$A_i = \frac{1}{J}(JU^k)\frac{\partial u_i}{\partial \xi^k} = \frac{1}{J}\left[B_i + \alpha(\Delta \xi^k)^3 \left|JU^k\right| \delta'^4_k u_i\right]. \tag{14}$$

In Eq. (14), B_i is the fourth-order central FDM discretization on the advection term; in accordance with the suggestion of Morinishi et al. (1998), the following formulation was used in this study:

$$B_i = \frac{9}{8}\overline{(JU)^k \delta_{1k} u_i}^{1k} - \frac{1}{8}\overline{(JU)^k \delta_{3k} u_i}^{3k}. \tag{15}$$

The second term in Eq. (14) is the numerical viscosity and α was set to 1 in this study, and this corresponds to utilizing the uniformly third-order polynomial interpolation algorithm (Leonard et al., 1995). Eq. (13) was solved with the successive over-relaxation (SOR) method. The predicted velocity, u^P, was transformed to the contravariant component and was interpolated at the staggered position after multiplication by J,

$$(JU^j)^P = \overline{J\frac{\partial \xi^j}{\partial x_i} u_i^P}^j. \tag{16}$$

Using $(JU^j)^P$ of Eq. (16), the Poisson equation on the potential ψ is expressed as

$$\frac{\delta_j (JU^j)^P}{\Delta t} = -\delta_j \left(\overline{\gamma^{jk}}^j \delta_k \psi \right). \tag{17}$$

This equation is derived such that JU^j at the next step,

$$(JU^j)^{n+1} = (JU^j)^P - \Delta t \overline{\gamma^{jk}}^j \delta_k \psi, \tag{18}$$

must satisfy the continuity on JU^j (Eq. (8)). Eq. (17) was also solved by the SOR method in this study. Using ψ obtained from Eq. (17), the velocity at the next step was corrected as

$$u_i^{n+1} = u_i^P + \frac{\partial \xi^k}{\partial x_i} \overline{\delta_k \psi}^k, \tag{19}$$

and P at the next step was estimated by computing

$$P^{n+1} = P^n - \frac{\psi}{\Delta t} + \frac{1}{2J}\left(\frac{1}{\mathrm{Re}} + \frac{1}{\mathrm{Re}_t} \right) \delta_k \left(\overline{\gamma^{kl}}^k \delta_l \psi \right). \tag{20}$$

2.2. Grid system and boundary conditions

The flow around two circular cylinders in tandem arrangement was simulated in an elliptic-column space. This physical space was discretized with an O-type grid system, and Fig. 1 shows the schematic of the section of the grid system. The O-type grid system had the major axis of $60D$, the minor axis of $30D$ and the thickness of D. In the Cartesian coordinates in the physical space, the origin was located at the center between the two cylinder-sections and on a side plane of the grid system; the x_1-, x_2- and x_3-axis were along the streamwise direction, transverse to the streamwise direction and along the cylinder span, respectively. The computational coordinates were assigned in terms of body-conformed coordinates ξ^k. This 3-D grid system was constructed as follows. A 2-D grid system was built by solving the Poisson equation (Thompson et al., 1977; Steger and Sorenson, 1979) in the x_1–x_2 plane. The 3-D grid system was organized by just aligning the 2-D grids along the x_3-axis. The number of grids on the circumference of each circular cylinder was 200 and that in the cylinder direction was 26. The number of grids on Γ_1 and Γ_2 in Fig. 1 varied from 51 to 131 linearly on L/D. Fig. 2 shows a close-up of the x_3-slice of the 3-D grid system in the case of $L/D = 2$.

As shown in Fig. 1, the no-slip boundary condition was specified on the surfaces of the cylinders, and the in-flow boundary condition was set to $u_1 = 1$, $u_2 = u_3 = 0$. An advection-viscous condition suggested by Miyauchi et al. (1996) was applied to the out-flow boundary condition in this study:

$$\frac{\partial u_i}{\partial t} + u_m \frac{\partial u_i}{\partial x_j} = \frac{1}{\mathrm{Re}} \frac{\partial^2 u_i}{\partial x_j^2}. \tag{21}$$

Although the zero velocity-gradient condition has been commonly used as the out-flow boundary condition, Miyauchi et al. carried out the 2-D simulation on the behavior of a vortex in uniform flow and showed that this

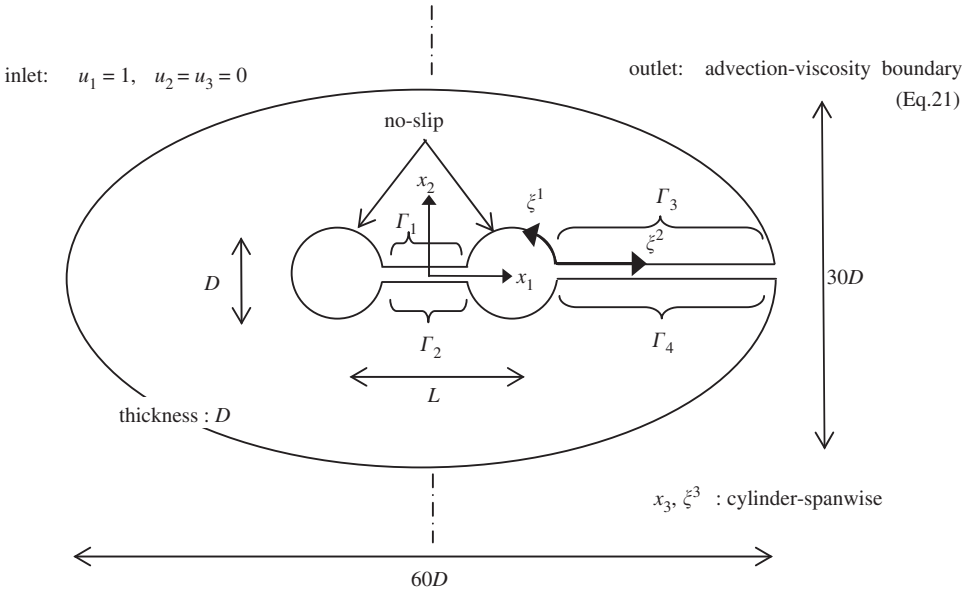

Fig. 1. Physical space around two circular cylinders in tandem arrangement, the coordinate system and the boundary conditions.

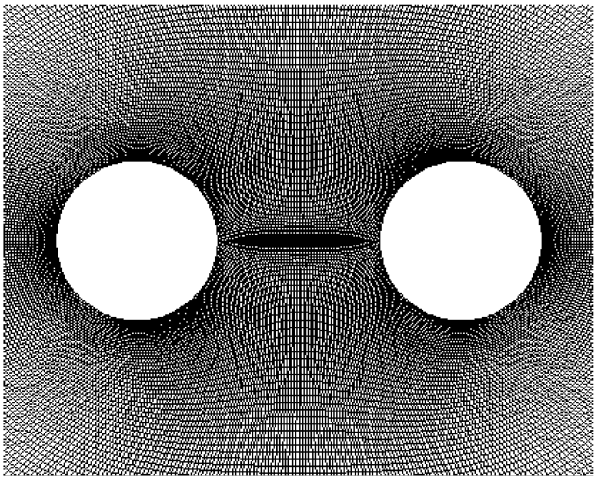

Fig. 2. Close-up view of x_3-slice of grid system in the case of $L/D = 2$.

boundary condition caused unphysical flow fluctuations around the vortex. In addition to the zero velocity-gradient condition, they tested four out-flow boundary conditions. The first boundary condition was an advection-inviscid condition where the approach-flow speed was used as the advection velocity, and the second one was an advection-inviscid condition where local velocities were used to the advection velocity. The third and fourth ones were the advection-viscous conditions which were the viscous versions of the first and the second conditions, respectively. Comparing the results for these four cases, they suggested that the third boundary condition corresponding to Eq. (21) with $u_m = 1$ approximated the flow fields near the out-flow boundary adequately, and this boundary condition was adopted in the present study. On the other hand, in Fig. 1, the periodic boundary condition was given between Γ_1 and Γ_2 as well as between Γ_3 and Γ_4. Also, between the x_1–x_2 plane at $x_3 = 0$ and that at $x_3 = D$, the periodic boundary condition was used. The computation was impulsively started, i.e., the initial condition of flow was set to $u_1 = 1$, $u_2 = u_3 = 0$ and $P = 0$.

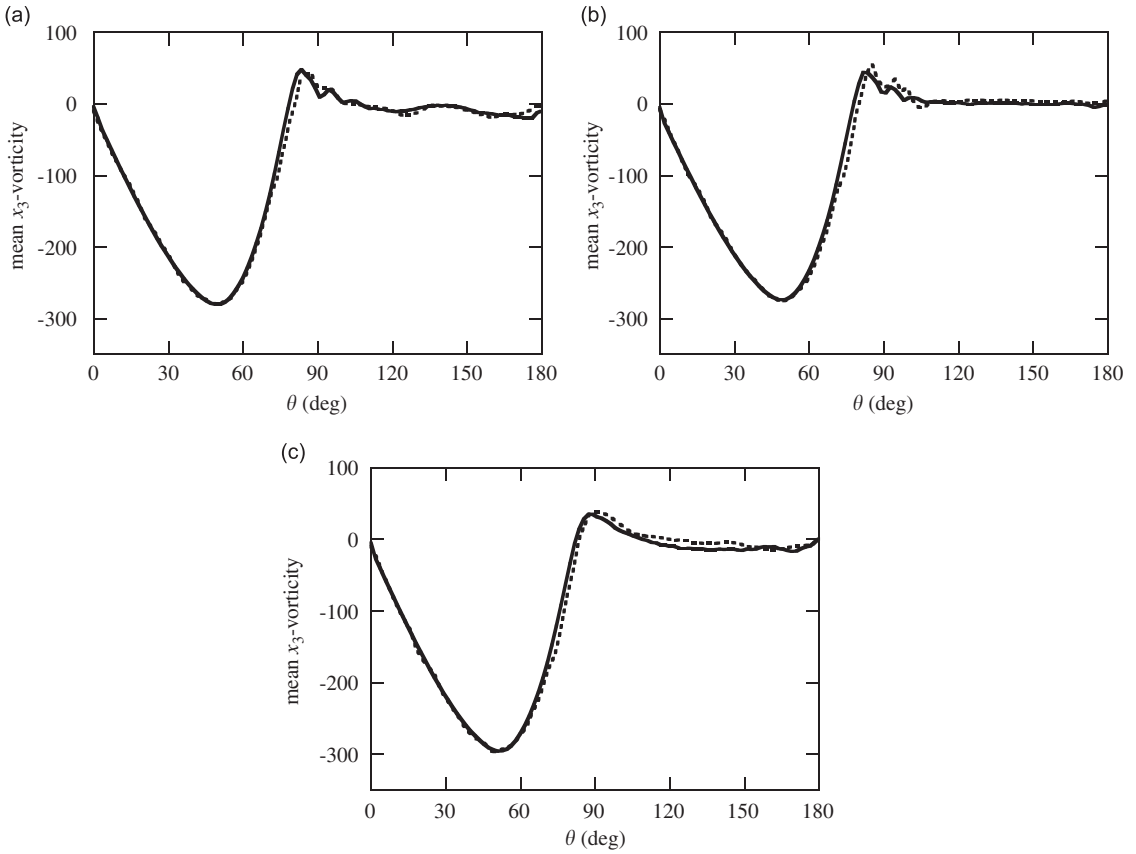

Fig. 3. Comparison of mean x_3-vorticity on the upper side surface of the upstream cylinder between the present grid case and the coarse grid case: (a) $L/D = 2$; (b) $L/D = 3$; (c) $L/D = 4$. θ: angle from the upstream side of the cylinder. Solid line: present grid case. Dashed line: coarse grid case.

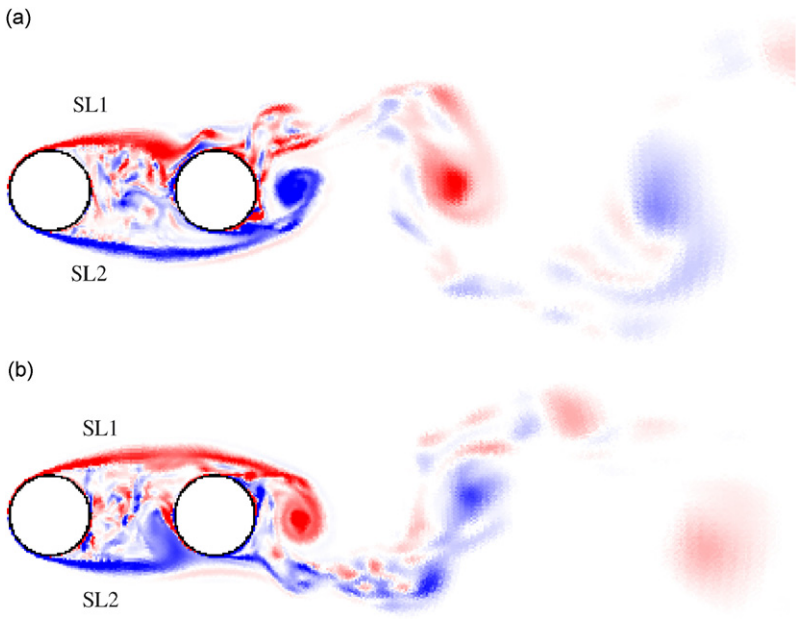

Fig. 4. Instantaneous vorticity distributions at middle of cylinder span in the case of $L/D = 2$: (a) reattachment of upper shear layer from the upstream cylinder, SL1, to the downstream cylinder; (b) reattachment of lower shear layer from the upstream cylinder, SL2, to the downstream cylinder.

Table 1
Numbers of grid points used for the grid-dependency tests

L/D	ξ^1-axis		ξ^2-axis	ξ^3-axis
	Present grid	Coarse grid		
2	501	351	150	26
3	551	401		
4	601	451		

The grid-number dependency was tested for the cases of $L/D = 2$, 3 and 4, comparing the x_3 component of vorticity obtained from the adopted grids with those from coarse grids, as shown in Fig. 3. Table 1 shows the number of grid points used for the tests. Fig. 3 shows that the adopted grid is adequate to represent the flow field.

3. Numerical results

3.1. Vorticity distribution

Fig. 4(a) shows a contour of instantaneous x_3-vorticity at the middle of the cylinder span in the case of $L/D = 2$. Vortices were not formed from the upstream cylinder. The upper side shear layer separated from the upstream cylinder, marked as 'SL1' in the figure, reattached to the downstream one, and the other shear layer 'SL2' connected to a vortex formed in the wake of the downstream. This vortex convected as the time passed, and inversely to Fig. 4(a), SL1 was detached from the downstream cylinder as shown in Fig. 4(b); i.e., these shear layers move up and down in phase and reattach alternately to the downstream cylinder. Synchronizing with this alternate reattachment of the shear layers, the alternate vortices are formed in the wake of the downstream cylinder. These flow characteristics are almost consistent with the those obtained by Zdravkovich (1987, 2003) and Igarashi (1981). However, the flow classification by Igarashi (1981) showed that the quasi-steady vortices are also formed between the cylinders in the case of $L/D = 2$ around the Re in this study. In the present study, although small vortices were formed intermittently around the front of the downstream cylinder due to the reaction of the shear layer reattachment as seen in Fig. 4(b), these vortices did not developed but disappeared. On the other hand, the vorticity distribution at $L/D = 2.5$ is shown in Fig. 5. The flow was almost the same as that in the case of $L/D = 2$, while the width of the shear layer movement was narrower than that at $L/D = 2$. A point of difference from the case of $L/D = 2$ is that the reattaching shear layer became unstable and fluctuated.

At $L/D = 3$, the shear layer movement as observed at $L/D = 2$ did not appear, and two flow patterns were observed. Fig. 6(a) shows one of them, in which both shear layers from the upstream cylinder symmetrically reattached to the downstream one. The wake of the downstream cylinder was highly turbulent and the vortex formation was not identifiable; the whole downstream cylinder wake fluctuated weakly. In the other flow pattern, as shown in Fig. 6(b), small vortices were formed in the space between the cylinders and convected toward the downstream cylinder. In this case, vortices were formed in the wake of the downstream cylinder, although their structure was not well organized. The latter flow pattern was dominant and the former one was intermittently observed. According to the flow classification by Igarashi (1981), both shear layer reattachment and vortex formation from the upstream cylinder can be present at this L/D value, and Igarashi called this a bistable flow. Although the vortices shed from the upstream cylinder were not of large scale in this study, the computed flows are thought to correspond to the bistable flow.

As shown in Fig. 7, at $L/D \geqslant 3.25$, the shear layers from the upstream cylinder did not reattach to the downstream one, and the vortices were alternately shed from the upstream cylinder; the critical spacing obtained in the present study was $L/D = 3.25$. Because of impingement of the vortices from the upstream cylinder on the downstream one, the flow near the downstream cylinder was highly unsteady.

On the other hand, it has been confirmed that the binary vortex street (Williamson, 1985; Zdravkovich, 2003) is formed when the L/D value is more than the critical spacing and is less than 6. Fig. 8(a) shows a vorticity distribution at $L/D = 4$, in which we can observe that a vortex (or eddy) shed from the upstream cylinder, marked as 'E_u', approaches the downstream cylinder. This vortex impinges the downstream cylinder and deforms as observed in Fig. 8(b), and the flow became highly unsteady due to the impingement as well as due to the friction on the surface of the downstream cylinder. Another small vortex (or eddy), marked as 'E_d' in Fig. 8(b), was also formed in the wake of the downstream cylinder. Successively, in Fig. 8(c), the merging of E_d and E_u was observed in the wake of the downstream cylinder,

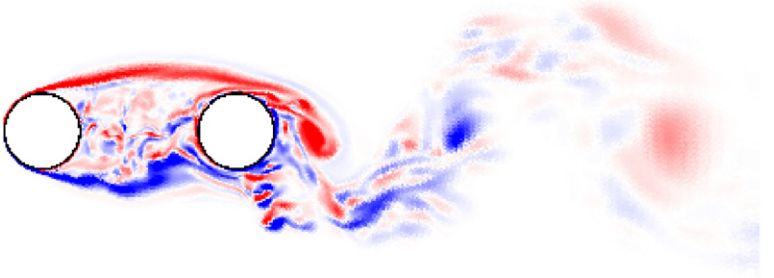

Fig. 5. Instantaneous vorticity distribution at middle of cylinder span in the case of $L/D = 2.5$. Fluctuating shear layer from the upstream cylinder reattaches to the downstream cylinder.

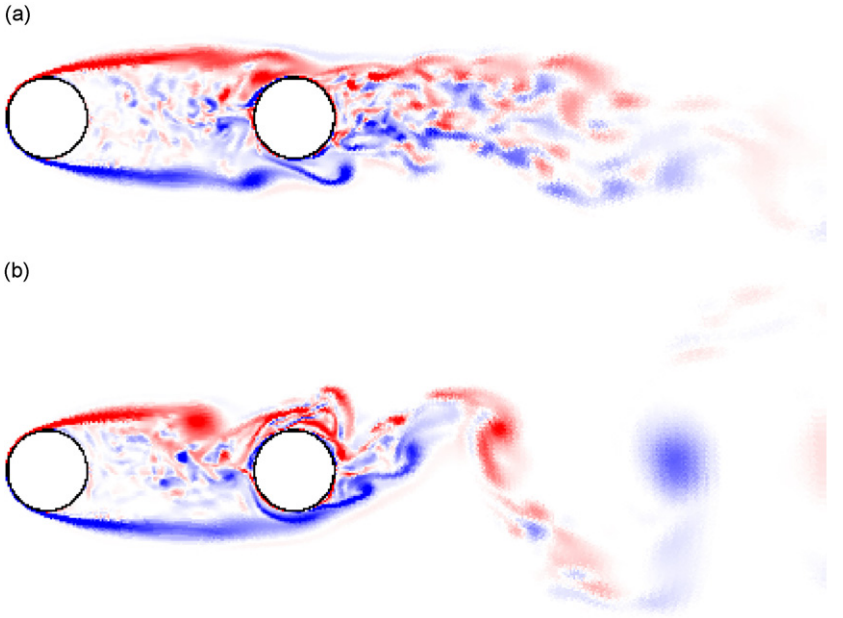

Fig. 6. Instantaneous vorticity distributions at middle of cylinder span in the case of $L/D = 3$: (a) symmetrical reattachment of shear layers from the upstream cylinder to the downstream cylinder and highly unsteady wake of the downstream cylinder; (b) small vortex generated from shear layer from the upstream cylinder.

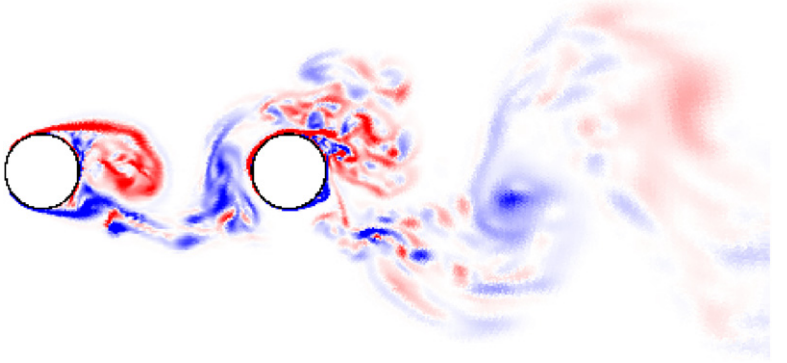

Fig. 7. Instantaneous vorticity distribution at middle of cylinder span in the case of $L/D = 3.25$. Vortices are formed not only from the downstream cylinder but also from the upstream cylinder.

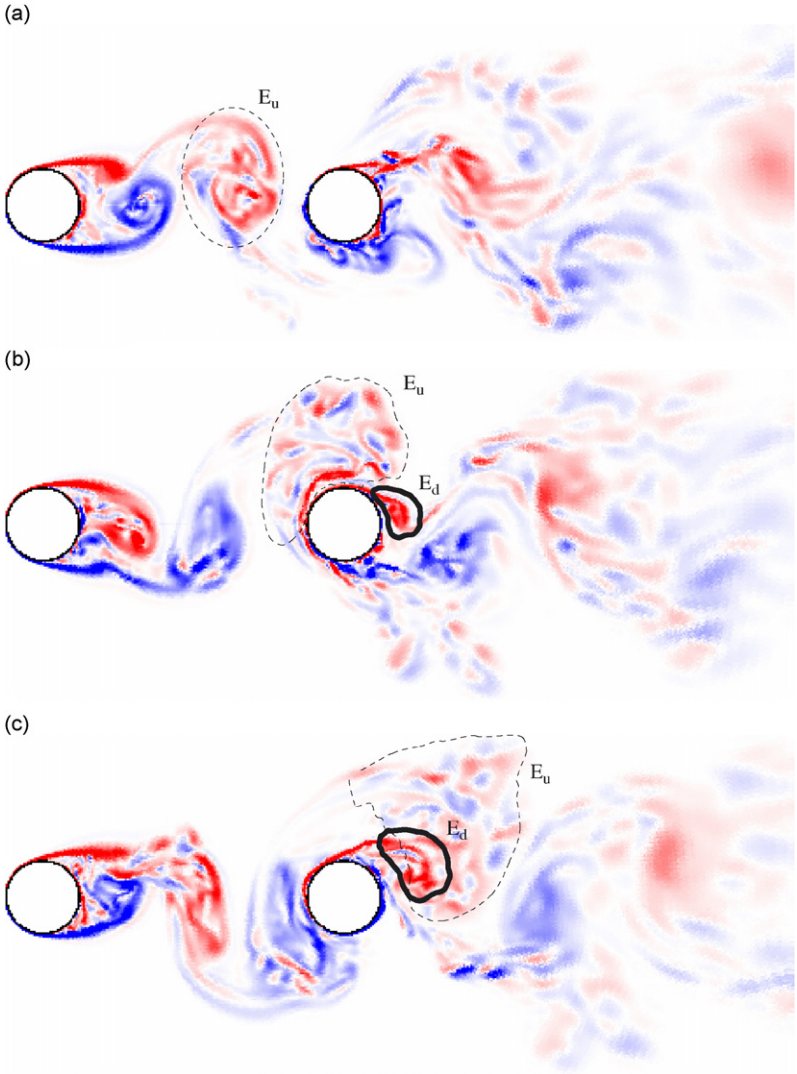

Fig. 8. Instantaneous vorticity distributions at middle of cylinder span in the case of $L/D = 4$: (a) vortex shed from the upstream cylinder, E_u, approaching to the downstream cylinder; (b) impingement of the vortex from the upstream cylinder onto the downstream cylinder and formation of a small vortex, E_d, in the wake of the downstream cylinder; (c) merging of both vortices and the convection.

although the vortex pairs were not clearly formed. This synchronized behavior of the two vortices was observed in the cases of $L/D \geqslant 3.25$. However, the degree of the mixture of these vortices depended on the strengths of the vortices either from the upstream cylinder or from the downstream one, and it also depended on the angle of the vortex impingement on the downstream-cylinder surface. The relationship between this synchronized behavior of the two vortices and the lift force acting on the downstream cylinder is investigated in Section 3.3.3.

3.2. Pressure distribution on circular cylinders

The pressure distributions on the surface of the cylinders at $L/D = 2$, 2.5, 3 and 4 are shown in Figs. 9–12, respectively. The mean pressure coefficient, $\overline{C_p}$, is shown in part (a) of these figures and the r.m.s. pressure coefficient, C_p', is in part (b). The symbol θ for the horizontal axis denotes the angle from the upstream side of the cylinder. The dashed line represents the pressure coefficients of the upstream cylinder and the solid line is for the downstream one. Additionally, the experimental results existing in the literature, at which the order of Re is approximately the same as

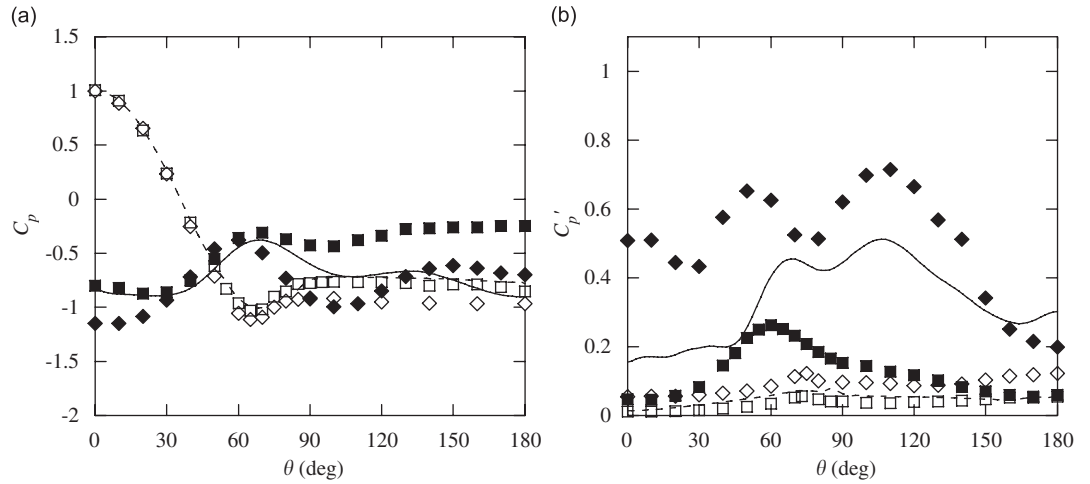

Fig. 9. Pressure distributions on the cylinder surfaces at $L/D = 2$: (a) mean pressure coefficients; (b) r.m.s. pressure coefficients. Dashed line: upstream cylinder in the present study. Solid line: downstream cylinder in the present study. Open symbol: upstream cylinder. Solid symbol: downstream cylinder. □ or ■, Ljungkrona et al. (1991) ($\mathrm{Re} = 2 \times 10^4$); ◇ or ◆, Moriya et al. (1983) ($\mathrm{Re} = 9 \times 10^4$).

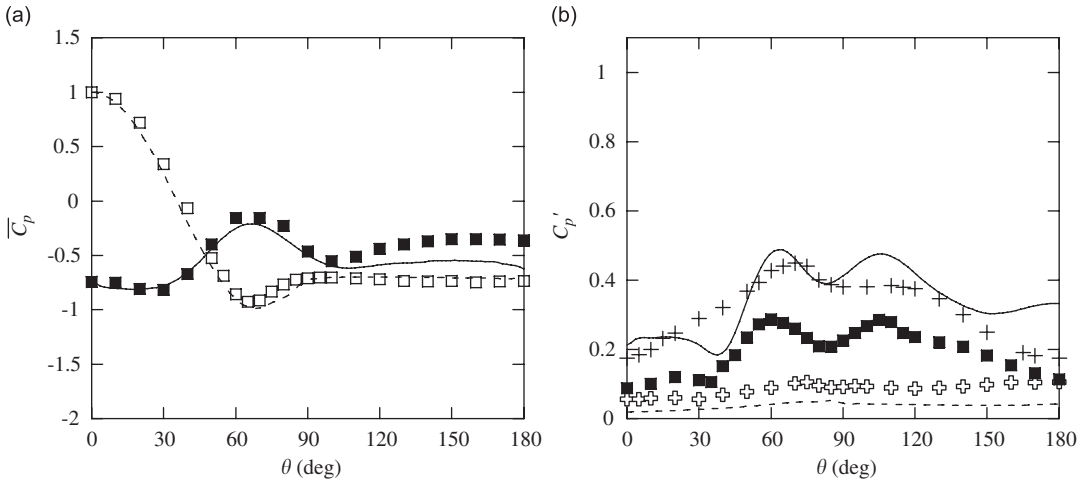

Fig. 10. Pressure distributions on the cylinder surfaces at $L/D = 2.5$: (a) mean pressure coefficients; (b) r.m.s. pressure coefficients. Dashed line: upstream cylinder in the present study. Solid line: downstream cylinder in the present study. Open symbol: upstream cylinder. Solid symbol: downstream cylinder. □ or ■, Ljungkrona et al. (1991) ($\mathrm{Re} = 2 \times 10^4$); ✣ or +, Igarashi (1981) ($\mathrm{Re} = 3.5 \times 10^4$).

the present study, are plotted in these figures for comparison: the open symbols are the values of the upstream cylinder and the solid symbols are for the downstream one.

Fig. 9(a) shows the $\overline{C_p}$ distribution at $L/D = 2$, and the numerical results for the upstream cylinder agreed well with the experimental results at $\mathrm{Re} = 2 \times 10^4$ by Ljungkrona et al. (1991). For the downstream cylinder, while we can see the agreement with their experimental results in the range of $0 \leqslant \theta < 80^\circ$, the $\overline{C_p}$ values at $\theta \geqslant 80^\circ$ are less than the experimental values. Similarly, in the case of $L/D = 2.5$ shown in Fig. 10(a), our $\overline{C_p}$ values are almost consistent with the experimental ones, and those of the downstream cylinder at $\theta \geqslant 110^\circ$ are slightly lower than the results by Ljungkrona et al. At $L/D = 3$ (Fig. 11(a)), our $\overline{C_p}$ values approximately agree with the results by Ljungkrona et al. Throughout Figs. 9(a)–11(a), in the range of $L/D \leqslant 3$, the $\overline{C_p}$ distributions are almost independent of the L/D value. This is because the flow patterns at $L/D \leqslant 3$ are similar; the shear layer from the upstream cylinder reattach to the downstream cylinder and no distinct vortices are shed from the upstream cylinder (Figs. 4–6). On the other hand, while

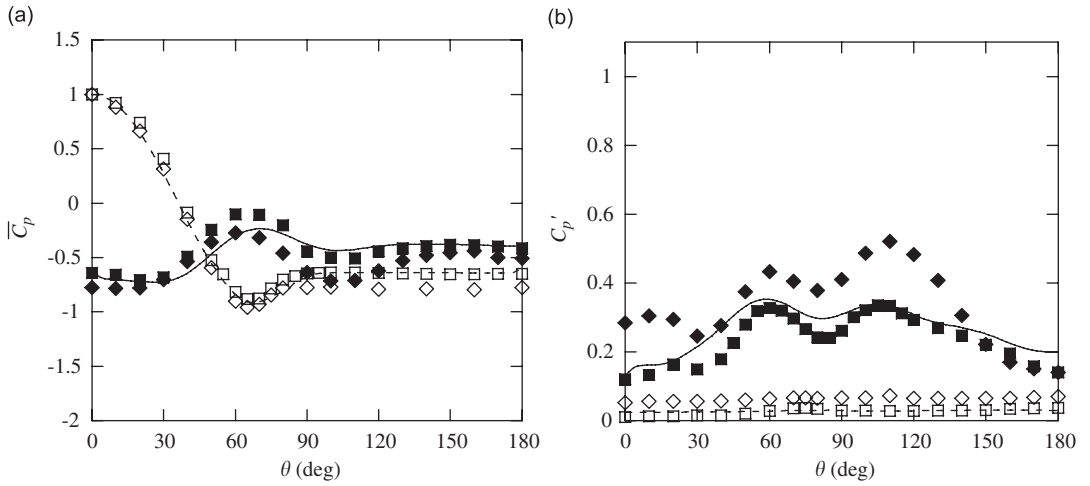

Fig. 11. Pressure distributions on the cylinder surfaces at $L/D = 3$: (a) mean pressure coefficients; (b) r.m.s. pressure coefficients. Dashed line: upstream cylinder in the present study. Solid line: downstream cylinder in the present study. Open symbol: upstream cylinder. Solid symbol: downstream cylinder. □ or ■, Ljungkrona et al. (1991) ($\mathrm{Re} = 2 \times 10^4$); ◇ or ◆, Moriya et al. (1983) ($\mathrm{Re} = 9 \times 10^4$).

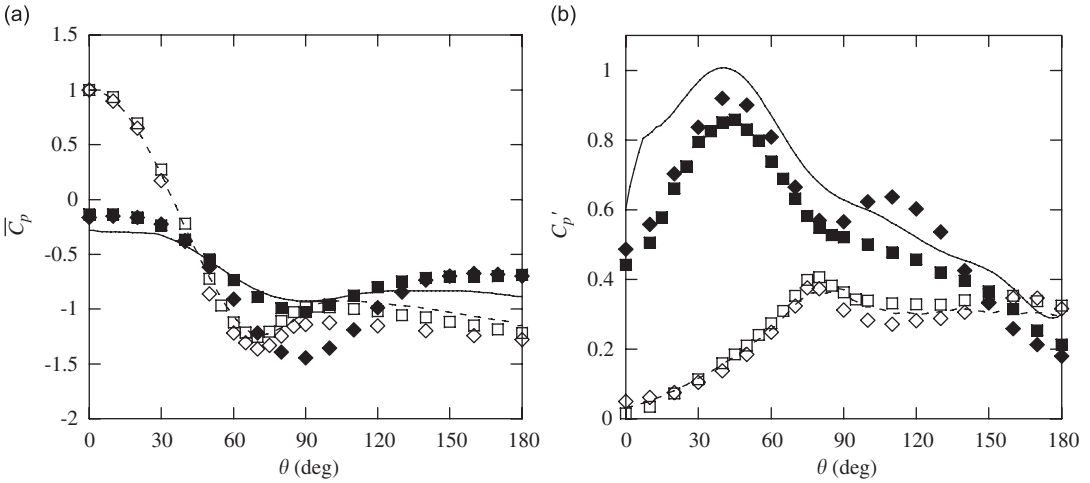

Fig. 12. Pressure distributions on the cylinder surfaces at $L/D = 4$: (a) mean pressure coefficients; (b) r.m.s. pressure coefficients . Dashed line: upstream cylinder in the present study. Solid line: downstream cylinder in the present study. Open symbol: upstream cylinder. Solid symbol: downstream cylinder. □ or ■, Ljungkrona et al. (1991) ($\mathrm{Re} = 2 \times 10^4$); ◇ or ◆, Moriya et al. (1983) ($\mathrm{Re} = 9 \times 10^4$).

there is a peak around $\theta = 70^\circ$ in the $\overline{C_p}$ distribution of the downstream cylinder for $L/D \leqslant 3$, this is not found in the case of $L/D = 4$ (Fig. 12(a)) where vortices are shed from the upstream cylinder. This peak of $\overline{C_p}$ is due to the reattachment of the upstream-cylinder shear layer to the downstream one, and the value of θ where the peak value takes place corresponds to the reattachment position on the surface of the downstream cylinder. Fig. 13 shows the reattachment angle on the downstream cylinder, θ_r, and the value of the mean pressure coefficient at the peak, $\overline{C_{pr}}$, versus L/D. For comparison, the experimental results at $\mathrm{Re} = 6.5 \times 10^4$ by Moriya et al. (2002) are also plotted in the figure. The open symbols represent θ_r corresponding to the left vertical axis and the solid symbols denote $\overline{C_{pr}}$ corresponding to the right axis. The results by Moriya et al. indicated that there was a correlation between θ_r and $\overline{C_{pr}}$: the θ_r value became large as the $\overline{C_{pr}}$ value decreased. The results of the present study show the same trend although the θ_r values of the present study are larger than the results of Moriya et al.

Fig. 9(b) shows the C_p' distribution at $L/D = 2$, and the C_p' values on the upstream cylinder agree with the experimental results by Ljungkrona et al. (1991). However, the C_p' values on the downstream cylinder are larger than

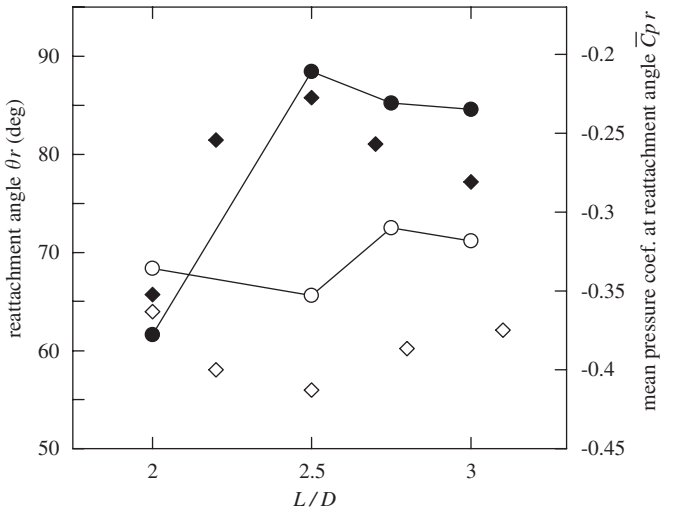

Fig. 13. Relationship between the shear layer reattachment angle on the surface of downstream cylinder and the mean pressure coefficient at the reattachment angle. Open symbol: reattachment angle. Solid symbol: mean pressure coefficients at the reattachment angles. ● or ○, present study; ◆ or ◇, Moriya et al. (2002) ($\mathrm{Re} = 6.5 \times 10^4$).

those by Ljungkrona et al. and are smaller than those at $\mathrm{Re} = 9 \times 10^4$ by Moriya et al. (1983). Furthermore, the C_p' distribution of the downstream cylinder possesses two peaks around $\theta = 70^\circ$ and 110° in this study. The C_p' distribution obtained by Moriya et al. also showed two peaks around $\theta = 50^\circ$ and 110°, while that by Ljungkrona et al. had a single peak around $\theta = 60^\circ$. Ljungkrona et al. investigated the effects of Re on the C_p' values at $L/D = 2$. They measured C_p' on the downstream cylinder at $\mathrm{Re} = 6 \times 10^4$ and compared with those at $\mathrm{Re} = 2 \times 10^4$; the result indicated that the C_p' values at $\mathrm{Re} = 6 \times 10^4$ were as large as those at $\mathrm{Re} = 9 \times 10^4$ by Moriya et al. and that the two peaks appeared in the C_p' distribution. According to their results, the C_p' values on the downstream cylinder at $L/D = 2$ are sensitive to Re and it is inferred that the difference in Re is a cause of the discrepancy between the C_p' values of the present computation and those of the experiment by Ljungkrona et al.

In addition to the Re-dependency, the other cause of this C_p' discrepancy may be the difference in the aspect ratio of the cylinder (span-wise length of the cylinder to cylinder diameter, l/D) between the present simulation and the experiments. While the l/D value was set to 1 in the present simulations, cylinders with larger l/D are used in experiments generally. Indeed, the l/D value of the cylinder used in the experiment by Ljungkrona et al. was 15.8. The aspect ratio of the cylinder affects the degree of the 3-D fluid motion around the cylinder.

In the case of $L/D = 2$, the shear layer from the upstream cylinder reattaches to the downstream cylinder, and this generates unstable fluid fluctuations; the characteristics of the velocity and the pressure fluctuations around the downstream cylinder can be susceptible to variations in the aspect ratio. As the L/D value increased (Figs. 10(b) and 11(b)), the C_p' magnitude on the downstream cylinder decreased. This corresponds to the fact that the movement width of the shear layers from the upstream cylinder, as was discussed in Section 3.1, becomes small as L/D increases. On the other hand, at $L/D = 4$, as shown in Fig. 12(b), the C_p' values on the upstream cylinder became much larger than those in the cases of $L/D \leqslant 3$. In the cases of $L/D > 3$, vortices were shed from the upstream cylinder. The vortex formation causes fluid fluctuations around the cylinder, and this results in the C_p' values on the upstream cylinder becoming larger than those in the cases of $L/D \leqslant 3$. The C_p' values on the downstream cylinder at $L/D = 4$ also became larger than those in the cases of $L/D \leqslant 3$. The vortices shed from the upstream cylinder convect in the downstream direction and impinge the downstream cylinder; this vortex impingement drives the pressure fluctuations on the surface of the downstream cylinder to be large. However, the C_p' values of the downstream cylinder were larger than those of the experimental results. Itoh and Himeno (2002) performed numerical simulations on the flow around two circular cylinders in tandem arrangements using a multi-layer grid system, and they obtained a similar C_p' overestimation on the downstream cylinder. As seen in Fig. 12(b), the C_p' values on the upstream cylinder agree with the experimental results, and this implies that a cause of the C_p' overestimation can be found in the process of the vortex convection from the upstream cylinder to the downstream one. Because the vortices from the upstream cylinder impinge the downstream cylinder, the 3-D effects are predominantly greater than for the cases of $L/D \leqslant 3$. Similar to the discussion on C_p' in the case of $L/D = 2$, it is then conjectured that the small l/D resulted in the C_p' overestimation of the downstream cylinder. The large C_p' values on the downstream cylinder indicate that the cylinder length used in the present simulations is not long

enough for the 3-D flow field to have developed. Further calculations using computational spaces with larger l and larger grids in the spanwise direction will be required to obtain the C_p' values close to experimental data.

3.3. Fluid forces

3.3.1. Drag force and lift force

Figs. 14(a) and (b) show the time histories of the lift coefficients, C_L, and the drag coefficients, C_D, at $L/D = 2$, respectively. The dotted line represents these coefficients of the upstream cylinder and the solid one is for the downstream cylinder. In Fig. 14(a), the C_L amplitude of the upstream cylinder is small relative to that of the downstream cylinder. No vortices are shed from the upstream cylinder, and the C_L fluctuation of the upstream cylinder is induced by the movement of the upstream-cylinder shear layers. The C_L fluctuation of the downstream cylinder is caused by the alternate reattachment of the upstream-cylinder shear layers, as well as by the vortex shedding from the downstream cylinder. In Fig. 14(b), compared with the C_D fluctuation of the downstream cylinder, that of the upstream cylinder is small. This is also due to no vortex formation from the upstream cylinder. Figs. 15(a) and (b) show the time histories of C_L and C_D at $L/D = 3$. The fluctuations of C_L and C_D for the upstream cylinder are smaller than those in the case of $L/D = 2$ and this is explained, as described in Section 3.1, by the width of the shear layer movement becoming small as the L/D value increases. A point to note is that the C_L fluctuation of the downstream cylinder is time dependent: the C_L fluctuations around $80 < t < 110$ in Fig. 15(a) are weak locally. This time range was where the flow pattern shown in Fig. 6(a) appeared: the wake of the downstream cylinder was highly unsteady and the vortex structure was not clearly formed in the wake of the downstream cylinder. These resulted in the C_L fluctuations of the downstream cylinder becoming small in this time range. Additionally, in Fig. 15(b), the local mean C_D of the downstream cylinder in the range of $80 < t < 110$ appeared to be slightly lower than that at the other times. At $L/D = 4$, as shown in Figs. 16(a) and (b), the fluctuations of C_L and C_D of the upstream cylinder were larger than those for $L/D = 2$ and 3 because the center-to-center spacing was large enough for vortices to be shed from the upstream cylinder. For the downstream cylinder, the fluctuations of C_L and C_D were also larger than the cases of $L/D = 2$ and 3. In Section 3.1, it was mentioned that the impingement of the vortex shed from the upstream cylinder on the downstream cylinder synchronized with the formation of a small vortex in the wake of the downstream cylinder. The fluid forces due to both of these two vortices act on the downstream cylinder simultaneously. In Fig. 16(b), the nonstationary fluctuations can be observed in the C_D time history of the downstream cylinder. This nonstationarity of the C_D fluctuation is caused by the variable strength of the vortices shed from the upstream cylinder as well as by the variable impingement-position on the downstream-cylinder surface.

The mean drag coefficients, $\overline{C_D}$, versus L/D are shown in Fig. 17. In the range of $L/D \leqslant 3$, the $\overline{C_D}$ values for both the upstream and downstream cylinders decrease as the L/D value increased, and they have a minimum at $L/D = 3$. At the critical spacing of $L/D = 3.25$, $\overline{C_D}$ jumps to higher values. The results of the present simulations mostly agree with the experimental results in the literature. However, while $\overline{C_D}$ of the downstream cylinder at $L/D = 2$ agrees with the experimental result at $\mathrm{Re} = 3.1 \times 10^4$ by Zdravkovich and Pridden (1977), it deviates from the other experimental results: e.g., the $\overline{C_D}$ values at $L/D = 2$ and 2.5 in this study are larger than the experimental results by Ljungkrona et al. (1991) for which the value of Re is close to the one used in the present study. The cause of this discrepancy is that, as shown in Fig. 9(a), the $\overline{C_p}$ values at $\theta \geqslant 90^\circ$ on the downstream cylinder in this study are less than those by Ljungkrona et al. Similar to the discussion on C_p' in Section 3.2, the disagreements of $\overline{C_p}$ and $\overline{C_D}$ are possibly related to the difference in the aspect ratio, l/D, between the present study and the experiment by Ljungkrona et al. The fluctuating lift coefficient, C_L', and the fluctuating drag coefficient, C_D', are shown in Figs. 18(a) and (b), respectively. Similar to $\overline{C_D}$ shown in Fig. 17, these coefficients increase sharply at the critical spacing. Although C_L' and C_D' for $L/D < 3.25$ are almost consistent with the experimental results by Moriya et al. (2002), those of the downstream cylinder for $L/D \geqslant 3.25$ are much larger than the experimental results. These disagreements result from the C_p' overestimation of the downstream cylinder for $L/D \geqslant 3.25$, as mentioned in Section 3.2.

3.3.2. Strouhal number

The Strouhal number, St, was obtained from the power spectrum of the downstream-cylinder C_L, and Fig. 19 shows the relationship between L/D and St. For $L/D < 3$, the St value decreases gradually as the L/D value is increased. At $L/D = 3$, as shown in Fig. 20, the power spectrum of C_L of the downstream cylinder exhibits two peaks at $fD/U = 0.155$ and 0.165, and both of the reduced frequencies are plotted in Fig. 19. The presence of these two vortex shedding frequencies results from the two flow patterns shown in Figs. 6(a) and (b). Because Fig. 6(a) indicated the instantaneous vorticity distribution at $t = 95.4$ in Fig. 15 where the C_L amplitude became small locally, the low frequency component in Fig. 20 can be due to the weak fluctuation of the downstream-cylinder wake as explained in Section 3.1. The high

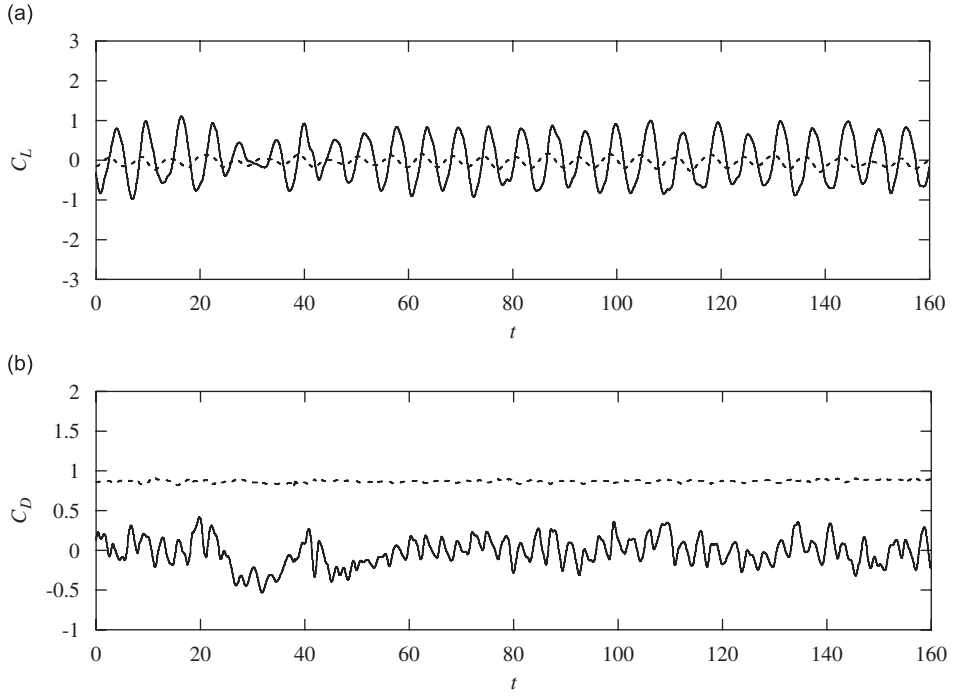

Fig. 14. Time histories of lift and drag forces acting on the cylinders at $L/D = 2$: (a) lift coefficient; (b) drag coefficient. Dashed line: upstream cylinder. Solid line: downstream cylinder.

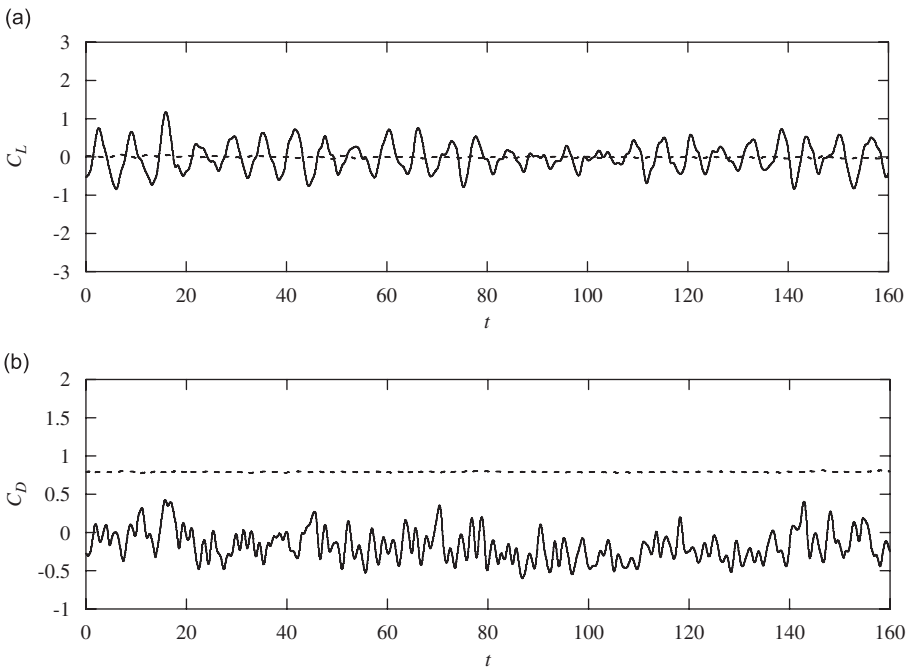

Fig. 15. Time histories of lift and drag forces acting on the cylinders at $L/D = 3$: (a) lift coefficient; (b) drag coefficient. Dashed line: upstream cylinder. Solid line: downstream cylinder.

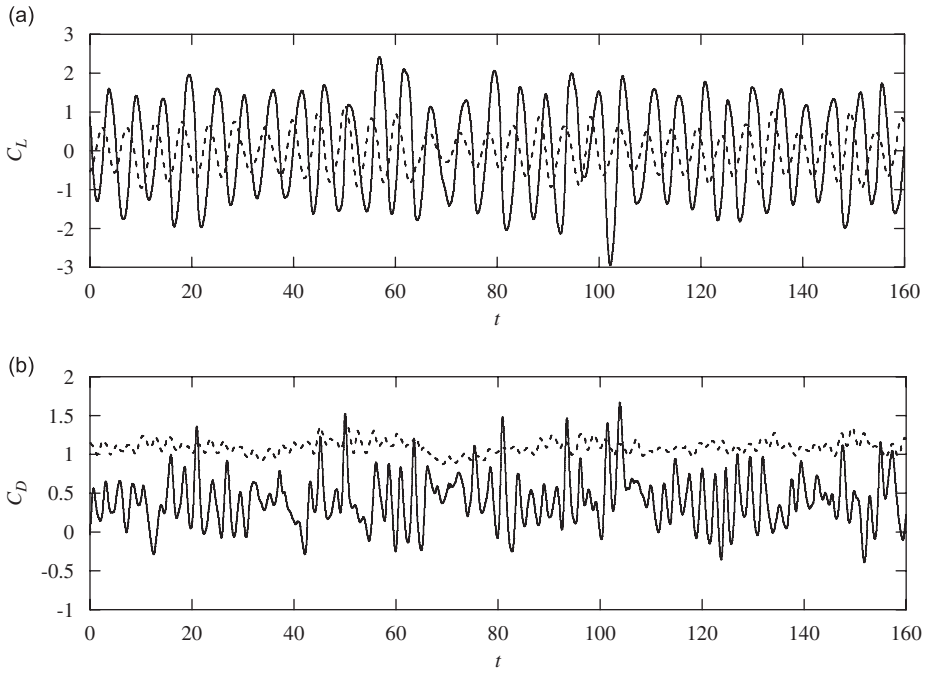

Fig. 16. Time histories of lift and drag forces acting on the cylinders at $L/D = 4$: (a) lift coefficient; (b) drag coefficient. Dashed line: upstream cylinder. Solid line: downstream cylinder.

frequency component in Fig. 20 corresponds to the C_L fluctuation due to the flow pattern in Fig. 6(b) ($t = 138.2$ in Fig. 15) which appeared dominantly. In Fig. 19, the value of St jumps to 0.172 at $L/D = 3.25$ and increases gradually as the L/D value is increased. The relationship between L/D and St in this study agreed approximately with the experimental results by Igarashi (1981).

3.3.3. *Convection of vortices shed from the upstream cylinder*

As described in Section 3.1, vortices were shed from the upstream cylinder in the cases of $L/D \geqslant 3.25$, and they impinged the downstream cylinder and mixed with the vortices formed in the near wake of the downstream cylinder. In this section, focusing on the relationship between the lift forces of the upstream and downstream cylinders, the characteristics of the convection of the vortices from the upstream cylinder are discussed.

Indicated in Fig. 21(a) is the instantaneous surface pressure distribution of the downstream cylinder at the middle of the cylinder span in the case of $L/D = 4$, at which the flow shown in Fig. 8(a) appeared ($t = 27.3$ in Fig. 16). The solid line outside the dotted circle represents negative pressure and the inner line represents positive pressure. The pressures on the upper side of the cylinder surface are positive due to the oncoming vortex shed from the upstream cylinder (E_u in Fig. 8(a)), and the lower side has negative pressures. Fig. 21(b) shows the instantaneous pressure distribution at which E_u impinged the downstream cylinder as in Fig. 8(b) ($t = 29.3$ in Fig. 16). The upper side of the downstream cylinder surface is covered by negative pressures, and the lift force is in the upward direction. The vortex formed in the wake of the downstream cylinder (E_d in Fig. 8(b)) also influenced the negative pressures. However, it is difficult to distinguish between the negative pressures by E_u and those by E_d. Comparing Fig. 8(b) with Fig. 21(b), it is conjectured that the negative pressures around $0 \leqslant \theta < 120^\circ$ are caused mainly by E_u and those around $120 \leqslant \theta < 220^\circ$ are due to E_d. The pair of E_u and E_d convected in the downstream direction (Fig. 8(c)), and the effect of these vortices on the downstream-cylinder surface pressure became weak; the upper side surface of the cylinder has positive pressures as shown in Fig. 21(c) ($t = 31.3$ in Fig. 16). While the pressure distributions varied depending on the angle of the vortex impingement on the downstream cylinder and on the strength of the vortices formed from each cylinder, the above-mentioned process of the pressures on the downstream-cylinder surface was repeated.

As found above, the negative pressures due to the vortices from both cylinders acted on the downstream cylinder simultaneously, and the dominant frequencies of the C_L fluctuations of both cylinders (St) were the same (e.g., Figs. 22(a) and (b)). It is inferred that the phase shift between the C_L fluctuation of the upstream cylinder and that of the

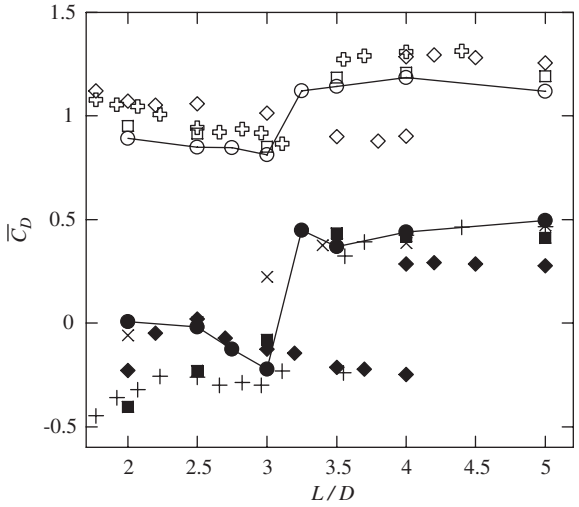

Fig. 17. Mean drag coefficients on the cylinders. Open symbol: upstream cylinder. Solid symbol: downstream cylinder. ● or ○, present study; □ or ■, Ljungkrona et al. (1991) ($Re = 2 \times 10^4$); ◆ or ◇, Moriya et al. (2002) ($Re = 6.5 \times 10^4$); ✣ or +, Igarashi (1981) ($Re = 3.55 \times 10^4$); ×, Zdravkovich and Pridden (1977) ($Re = 3.1 \times 10^4$).

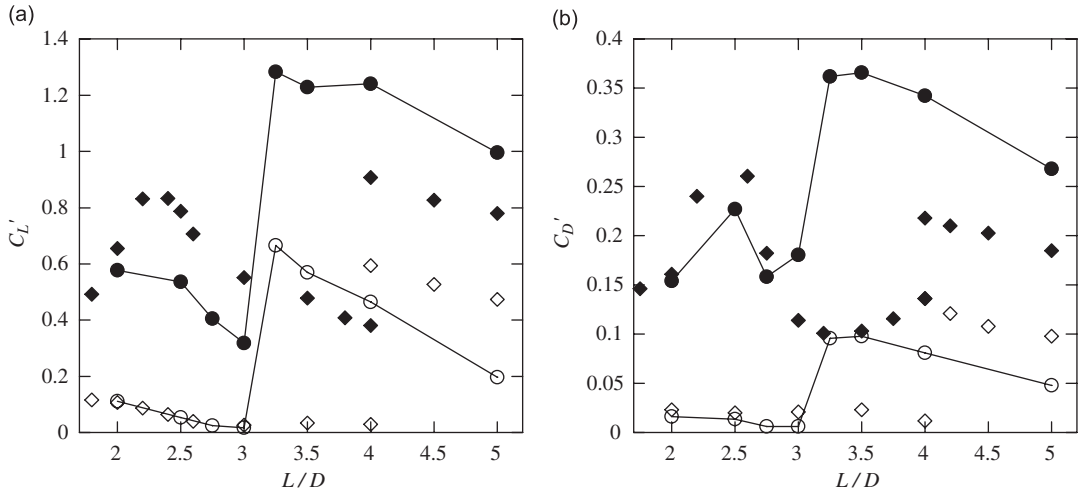

Fig. 18. Fluctuating lift and drag coefficients on the cylinders: (a) fluctuating lift coefficients; (b) fluctuating drag coefficients. Open symbol: upstream cylinder. Solid symbol: downstream cylinder. ● or ○, present study; ◆ or ◇, Moriya et al. (2002) ($Re = 6.5 \times 10^4$).

downstream one correlates with L/D. Fig. 23 shows the phase shifts, ϕ (rad), at St between the C_L fluctuations of both cylinders. Because no distinct vortices were shed from the upstream cylinder for $L/D \leqslant 3$, only ϕ values in the range of $L/D \geqslant 3.25$ are related to the vortex shedding from both cylinders. Additionally, ϕ values at $L/D = 3$ are not plotted in Fig. 23 because there is not a single dominant frequency in the downstream-cylinder C_L as shown in Fig. 19. Furthermore, the ϕ values at $L/D \geqslant 3.25$ were obtained as $\phi = \phi_c + 2\pi$, where ϕ_c is the phase shift at St obtained from the cross spectrum of C_L. For example, in Fig. 8(b), we can see that when E_u impinges the downstream cylinder and E_d is formed, a new vortex is shed from the upper side of the upstream cylinder: the ϕ_c value corresponds the phase shift between the upstream-cylinder lift due to the new vortex and the downstream-cylinder lift due to both E_d and E_u. On the other hand, the ϕ value indicates the phase shift between the upstream-cylinder lift at which E_u is shed from the upstream cylinder and the downstream-cylinder lift due to both E_d and E_u. Hence, the value of ϕ involves the period of time during which E_u convects from the upstream cylinder to the downstream one. Sakata and Kiya (1983) experimentally investigated the phase shifts between the C_L fluctuations of both cylinders at $Re = 10^5$ and suggested the

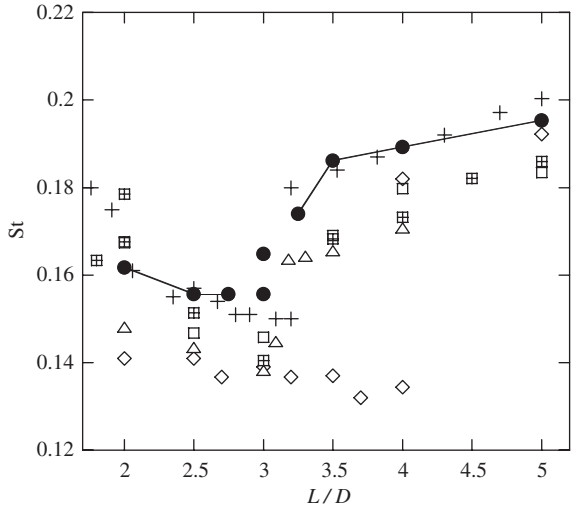

Fig. 19. Strouhal number. ●, present study; +, Igarashi (1981) ($Re = 2.2 \times 10^4$); □, Ljungkrona et al. (1991) ($Re = 2 \times 10^4$); ◇, Moriya et al. (2002) ($Re = 6.5 \times 10^4$); ⊞, Kiya et al. (1980) ($Re = 1.58 \times 10^4$); △, Ozono et al. (2001) ($Re = 3 \times 10^4$).

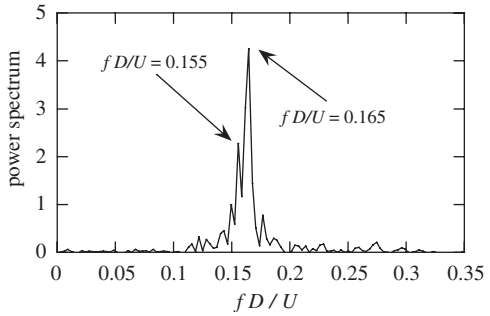

Fig. 20. Power spectrum of fluctuating lift of the downstream cylinder for $L/D = 3$.

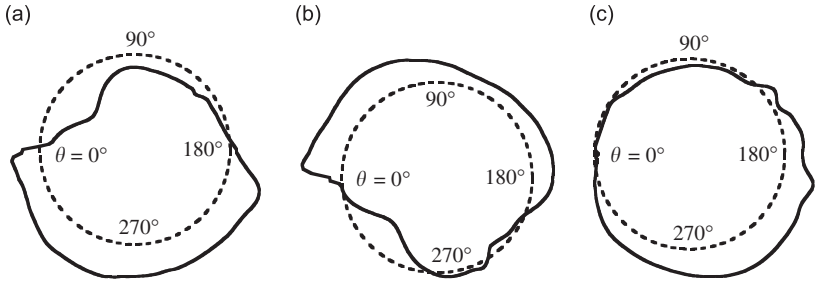

Fig. 21. Pressure coefficient distributions on the surface of the downstream cylinder at $L/D = 4$: (a) C_p at which the vorticity appeared as in Fig. 8 (a); (b) C_p at which the vorticity appeared as in Fig. 8 (b); (c) C_p at which the vorticity appeared as in Fig. 8 (c).

ϕ-L/D relationship as

$$\phi = 1.6\frac{L}{D} + 1.5 \text{ (rad)}. \tag{22}$$

The line for Eq. (22) is illustrated in Fig. 23 for comparison. The result of the present study indicates that ϕ is almost proportional to L/D and agrees with Eq. (22) in spite of the difference in Re. Using these ϕ values, the nondimensional

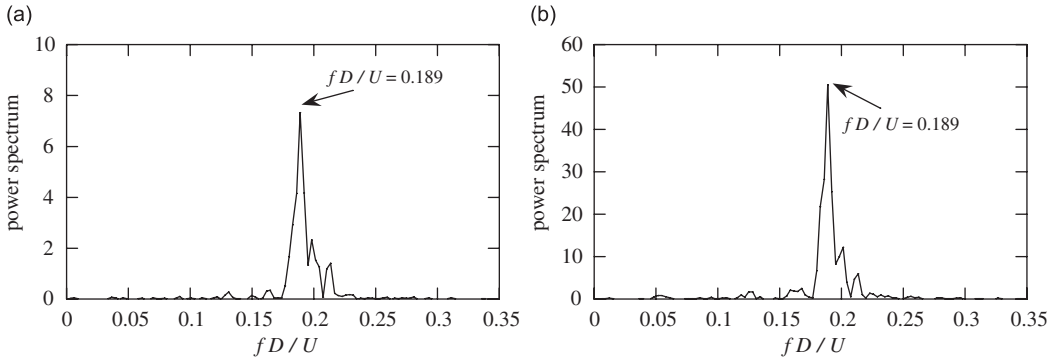

Fig. 22. Power spectra of fluctuating lift of the cylinders at $L/D = 4$: (a) upstream cylinder; (b) downstream cylinder.

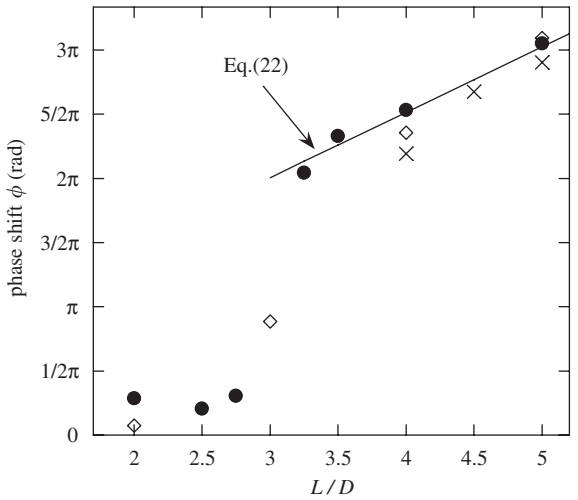

Fig. 23. Phase shift of fluctuating lift of the cylinders: ●, present study; ◇, Sakata and Kiya (1983) ($\mathrm{Re} = 10^5$); ×, Moriya et al. (2002) ($\mathrm{Re} = 6.5 \times 10^4$).

mean convection speed of the vortices shed from the upstream cylinder, U_{Eu}, can be estimated as

$$U_{Eu} = \frac{2\pi}{\phi}\mathrm{St}\frac{L}{D}. \tag{23}$$

The U_{Eu}–L/D relationship is shown in Fig. 24. The U_{Eu} values are in the range of 54–63% of the approach-flow speed and have a weak L/D dependency. In the case of a single circular cylinder at which the Re value is around 10^4, it is known that the convection speed of the vortices is about 60–80% of the approach-flow speed. The vortices shed from the upstream cylinder then move onto the downstream cylinder at speeds lower than that in the case of a single cylinder. Because U_{Eu} is proportional to L/D, the value of U_{Eu} becomes close to that for a single cylinder with further increase in L/D.

4. Conclusions

Three-dimensional calculations on flows around two circular cylinders of the same diameter in tandem arrangements at a subcritical Reynolds number, $\mathrm{Re} = 2.2 \times 10^4$, were performed. The center-to-center spacing between the cylinders was varied from twice to five times the cylinder diameter. For $L/D < 3.25$, it was observed that vortices were shed only from the downstream cylinder. The shear layers separated from both sides of the upstream cylinder and reattached alternately to the downstream cylinder. Vortices were formed in the wake of the downstream cylinder, synchronizing to

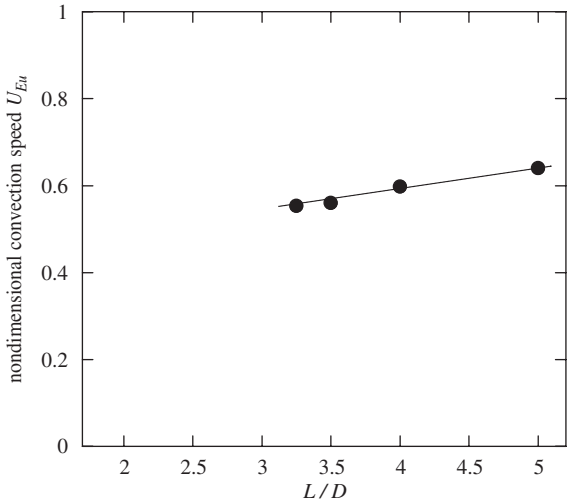

Fig. 24. Nondimensional mean convection speed of vortices shed from the upstream cylinder.

the alternate reattachments of the shear layers from the upstream cylinder. For $L/D \geqslant 3.25$, vortices were shed not only from the downstream cylinder but also from the upstream cylinder. The critical spacing was then obtained as $L/D = 3.25$ in this study. These relationships between the center-to-center spacing and the flow characteristics obtained in the present study were almost consistent with the experimental results reported in the literature. For the fluid dynamics forces acting on the cylinders, the results in this study showed agreement with the experimental data. However, for the downstream cylinder in the cases of $L/D \geqslant 3.25$, the fluctuating lift and drag as well as the pressure fluctuations were larger than the experimental data. These disagreements can be caused by the difference in the aspect ratio of the cylinder in the present study and in the experimental investigations. The relationship between the Strouhal number and L/D agreed approximately with the experimental result by Igarashi (1981) in which the Reynolds number was the same as that in the present simulations.

The characteristics of the vortices shed from the upstream cylinder in the cases of $L/D \geqslant 3.25$ were investigated. The vortices shed from the upstream cylinder convected in the stream-wise direction and impinged the downstream cylinder. When this vortex impingement occurred, a small vortex was formed in the wake of the downstream cylinder. The negative pressures due to these two vortices acted simultaneously on the surface of the downstream cylinder and caused the lift force to the downstream cylinder. Because of this synchronous work of these vortices for the lift force on the downstream cylinder, the dominant frequency of the lift fluctuation of the upstream cylinder coincided with that of the downstream one. Also, the phase shift between the fluctuating lift forces of the upstream and downstream cylinders correlated proportionally to L/D. The relationship between the phase shift and L/D in this study agreed with the linear function suggested by Sakata and Kiya (1983). Using the phase shift, the mean convection speed of the vortices shed from the upstream cylinder was estimated. It was found that the convection speeds were in the range of 54–63% of the approach-flow speed and were slightly proportional to L/D.

References

Akbari, M.H., Price, S.J., 2005. Numerical investigation of flow patterns for staggered cylinder pairs in cross-flow. Journal of Fluids and Structures 20, 533–554.

Amsden, A.A., Harlow, F.H., 1970. A simplified MAC technique for incompressible fluid flow calculations. Journal of Computational Physics 6, 322–325.

Bearman, P.W., Wadcock, A.J., 1973. The interaction between a pair of circular cylinders normal to a stream. Journal of Fluid Mechanics 61, 499–511.

Bokaian, A., Geoola, F., 1984. Wake-induced galloping of two interfering circular cylinders. Journal of Fluid Mechanics 146, 383–415.

Gu, Z., Sun, T., 1999. On interference between two circular cylinders in staggered arrangement at high subcritical Reynolds numbers. Journal of Wind Engineering and Industrial Aerodynamics 80, 287–309.

Igarashi, T., 1981. Characteristics of the flow around two circular cylinders arranged in tandem 1st report. Bulletin of JSME B 24, 323–331.

Igarashi, T., 1984. Characteristics of the flow around two circular cylinders arranged in tandem 2nd report: unique phenomenon at small spacing. Bulletin of JSME B 27, 2380–2387.

Itoh, Y., Himeno, R., 2002. Numerical accuracy of flow interference between two circular cylinders in tandem arrangement. In: Proceedings of 17th National Symposium on Wind Engineering, pp. 279–284 (in Japanese).

Jester, W., Kallinderis, Y., 2003. Numerical study of incompressible flow about fixed cylinder pairs. Journal of Fluids and Structures 17, 561–577.

Kajishima, T., Ohta, T., Okazaki, K., Miyake, Y., 1998. High-order finite-difference method for incompressible flows using collocated grid system. JSME International Journal Series B 41, 830–839.

King, R., Johns, D.J., 1976. Wake interaction experiments with two flexible circular cylinders in flowing water. Journal of Sound and Vibration 45, 259–283.

Kiya, M., Arie, M., Tamura, H., Mori, H., 1980. Vortex shedding from two circular cylinders in staggered arrangement. ASME Journal of Fluids Engineering 102, 166–173.

Leonard, B.P., Macvean, M.K., Lock, A.P., 1995. The flux integral method for multidimensional convection and diffusion. Applied Mathematical Modelling 19, 333–342.

Ljungkrona, L., Norberg, CH., Sundén, B., 1991. Free-stream turbulence and tube spacing effects on surface pressure fluctuations for two tubes in an in-line arrangement. Journal of Fluids and Structures 5, 701–727.

Meneghini, J.R., Saltara, F., Siqueira, C.L.R., Ferrari Jr., J.A., 2001. Numerical simulation of flow interference between two circular cylinders in tandem and side-by-side arrangements. Journal of Fluids and Structures 15, 327–350.

Mittal, S., Kumar, V., 2001. Flow-induced oscillations of two cylinders in tandem and staggered arrangements. Journal of Fluids and Structures 15, 717–736.

Mittal, S., Kumar, V., Raghuvanshi, A., 1997. Unsteady incompressible flows past two cylinders in tandem and staggered arrangements. International Journal for Numerical Methods in Fluids 25, 1315–1344.

Miyauchi, T., Tanahashi, M., Susuki, M., 1996. Inflow and outflow boundary conditions for direct numerical simulations. JSME International Journal Series B 39, 305–314.

Morinishi, Y., Lund, T.S., Vasilyev, O.V., Moin, P., 1998. Fully conservative higher order finite difference schemes for incompressible flow. Journal of Computational Physics 143, 90–124.

Moriya, M., Sakamoto, H., Kiya, M., Arie, M., 1983. Fluctuating pressures and forces on two circular cylinders in tandem arrangement. Transactions of the JSME 49, 1364–1374 (in Japanese).

Moriya, M., Alam, M., Takai, K., Sakamoto, H., 2002. Fluctuating fluid forces of two circular cylinders in tandem arrangement at close spacing. Transactions of the JSME 68, 1400–1406 (in Japanese).

Ozono, S., Oda, J., Yoshida, Y., Wakasugi, Y., 2001. Critical nature of the base pressure of the upstream circular cylinder in two staggered ones in cross-flow. Theoretical and Applied Mechanics 50, 335–340.

Rhie, C.M., Chow, W.L., 1983. A numerical study of the turbulent flow past a isolated airfoil with trailing edge separation. AIAA Journal 21, 1525–1532.

Sakata, I., Kiya, M., 1983. Fluctuating forces acting on two circular cylinders in tandem arrangement Part 2: Phase relations between fluctuating forces. Transactions of the JSME 49, 2618–2623 (in Japanese).

Steger, J.L., Sorenson, R.L., 1979. Automatic mesh-point clustering near a boundary in grid generation with elliptic partial differential equations. Journal of Computational Physics 33, 405–410.

Sumner, D., Price, S.J., Païdoussis, M.P., 2000. Flow-pattern identification for two staggered circular cylinders in cross-flow. Journal of Fluid Mechanics 411, 263–303.

Sumner, D., Richards, M.D., Akosile, O.O., 2005. Two staggered circular cylinders of equal diameter in cross-flow. Journal of Fluids and Structures 20, 255–276.

Sun, T.F., Gu, Z.F., He, D.X., Zhang, L.L., 1992. Fluctuating pressure on two circular cylinders at high Reynolds numbers. Journal of Wind Engineering and Industrial Aerodynamics 41–44, 577–588.

Thompson, J.F., Thames, F.C., Mastin, C.W., 1977. TOMCAT-A code for numerical generation of boundary-fitted curvilinear coordinates systems on field containing any number of arbitrary two-dimensional bodies. Journal of Computational Physics 24, 274–302.

Williamson, C.H.K., 1985. Evolution of a single wake behind a pair of bluff bodies. Journal of Fluid Mechanics 159, 1–18.

Zdravkovich, M.M., 1985. Flow induced oscillations of two interfering circular cylinders. Journal of Sound and Vibration 101, 511–521.

Zdravkovich, M.M., 1987. The effects of interference between circular cylinders in cross flow. Journal of Fluids and Structures 1, 239–261.

Zdravkovich, M.M., 2003. Flow Around Circular Cylinders Vol 2: Applications. Oxford University Press, Oxford.

Zdravkovich, M.M., Pridden, D.L., 1977. Interference between two circular cylinders; Series of unexpected discontinuities. Journal of Industrial Aerodynamics 2, 255–270.

Zhang, H., Melbourne, W.H., 1992. Interference between two circular cylinders in tandem in turbulent flow. Journal of Wind Engineering and Industrial Aerodynamics 41–44, 589–600.